RSC Advances

PAPER

View Article Online
View Journal | View Issue

Cite this: *RSC Adv.*, 2026, **16**, 15410

Anisotropic gold nanochains with dual-ligand interfaces for theranostic immune activation

Chungmo Yang, †[a] Young Ju Son,†[b] Sila Jin,[c] Yeonju Park,[c] Young Mee Jung, [acd] Seung Goo Kang*[e] and Hyuk Sang Yoo *[abc]

Antibody-dependent cellular cytotoxicity (ADCC) represents a key mechanism of cancer immunotherapy, yet conventional antibody-nanoparticle systems often suffer from limited Fc accessibility, random ligand orientation, and short circulation stability. To overcome these limitations, we developed a modular gold nanochain platform through end-to-end assembly of alkyne- and azido-functionalized gold nanorods using click chemistry. Each nanorod unit was selectively modified with folic acid or immunoglobulin G (IgG) Fc fragments to achieve spatially segregated tumor-targeting and immune-engaging functionalities. The resulting polyethylene glycol (PEG)-linked nanochains exhibited tunable length, excellent colloidal stability, and characteristic plasmonic coupling, enhancing both surface-enhanced Raman scattering (SERS) and near-infrared absorption. Cellular studies using folate receptor-positive KB cells confirmed receptor-mediated uptake and selective binding, while ADCC assays demonstrated significantly enhanced natural killer (NK) cell-mediated cytolysis compared to single nanorods and even the monoclonal antibody control (Herceptin). Mechanistically, the elongated morphology and multivalent Fc presentation facilitated stable immune synapse formation and improved effector cell recruitment. Collectively, this study establishes a versatile and biocompatible nanochain platform that integrates cancer targeting, immune activation, and optical imaging within a single construct, offering a promising direction for next-generation immunotheranostic nanomedicine.

Received 11th January 2026
Accepted 23rd February 2026

DOI: 10.1039/d6ra00281a

rsc.li/rsc-advances

1 Introduction

Cancer immunotherapy, particularly strategies leveraging antibody-dependent cellular cytotoxicity (ADCC), has become a fundamental pillar in modern oncology.[1–4] This mechanism is central to the success of targeted therapy using major clinical monoclonal antibodies (mAbs) such as rituximab, trastuzumab, and cetuximab.[5–7] However, the therapeutic potential of these mAbs is frequently constrained by significant pharmacological and immunological hurdles, including their short half-lives, which result in the requirement of frequent, high-dose regimens, off-target interactions with healthy tissues, and insufficient immune effector activation.[8,9] These hurdles stem from the difficulty exhibited by these soluble, monomeric antibodies in forming the high-avidity, clustered immune synapses that are required for robust natural killer (NK) cell activation.[10,11] First-generation nanotechnological approaches, such as those using spherical nanoparticles, solved pharmacokinetic issues by enhancing stability and circulation; however, they introduced a new, catastrophic failure.[12,13] The isotropic surface of spherical nanoparticles induces a stochastic immobilization of antibodies, leading to random orientations; quantitative mapping has revealed that under crowded conditions on spheres, Fc accessibility is significantly reduced as domains are buried against the particle surface or sterically masked.[12,14,15]

Nanotechnology-based delivery systems have been investigated as platforms to enhance antibody stability, prolong circulation, and improve tumor-specific localization.[16,17] To overcome the geometric and functional failures of spherical nanoparticles, research has pivoted to anisotropic (nonspherical) nanomaterials, including nanorods (NRs), nanowires, and nanochains.[18–20] The elongated geometry of these materials is an active design element that dictates biological function. At the macrolevel, anisotropy promotes improved vascular margination and tumor accumulation compared to those of their spherical counterparts, as their shape interacts differently corresponding to hemodynamics, leading to slower clearance and enhanced localization at the tumor site.[21,22] At the microlevel, this elongated architecture provides a unique scaffold for the

[a]*Institute for Molecular Science and Fusion Technology, Kangwon National University, Chuncheon 24341, Republic of Korea. E-mail: hsyoo@kangwon.ac.kr*

[b]*Department of Medical Biomaterials Engineering, Kangwon National University, Chuncheon 24341, Republic of Korea*

[c]*Kangwon Radiation Convergence Research Support Center, Kangwon National University, Chuncheon, 24341, Republic of Korea*

[d]*Department of Chemistry, Kangwon National University, Chuncheon 24341, Republic of Korea*

[e]*Department of Systems Immunology, Kangwon National University, Chuncheon 24341, Republic of Korea. E-mail: sgkang@kangwon.ac.kr*

† These authors contributed equally to this work.

multivalent and spatially controlled presentation of biological ligands.[23,24] This precise organization is the key to solving the Fc-accessibility crisis. For ADCC, the orientation and density of the Fc region are vital factors that determine the efficiency of Fc-receptor engagement in NK cells.[25–28] To overcome the geometric and functional failures of spherical nanoparticles, research has pivoted to anisotropic nanomaterials, including nanorods and nanochains. Unlike spherical surfaces, where random antibody orientation often leads to the burying of critical Fc domains, the elongated geometry of nanochains acts as an active design element. This 'linear-scaffold' architecture provides a unique template for the multivalent and spatially controlled presentation of ligands, facilitating the high-avidity, clustered immune synapses required for robust NK cell activation.

Building on the potential of anisotropic materials, prior studies have explored various geometries, each with distinct results and limitations.[29,30] For instance, although rigid NRs or nanowires offer elongated structures, their inflexible nature may not be optimal for dynamic cellular interactions, and their largescale synthesis can present challenges.[31] Nanochains, as a specific class, offer a unique set of advantages. By linking the NR building blocks with flexible polymeric linkers, these constructs gain structural adaptability.[32] Their flexibility is a key strength, enabling nanochains to dynamically adapt their configuration and conform to the membrane curvature on the cell surface. This modular assembly also enables a programmable presentation of distinct ligands in a way that can prevent steric hindrance, which is a critical factor for facilitating the stable immune synapse formation required for a potent ADCC.

This study summarizes the rational design of a modular gold nanochain platform to leverage these advantages. The gold nanochain was constructed *via* an end-to-end assembly of individual alkyne- and azido-functionalized gold NRs (GNRs) using click chemistry. The nanochain used in this study involved a dual-ligand strategy that achieved spatially segregated functionalities: folic acid (FA) for tumor targeting and immunoglobulin G (IgG) Fc fragments for immune engagement were placed on distinct NR units before assembly. The flexible and biocompatible platform demonstrated a tunable length and theranostic potential with characteristic plasmonic coupling that improved surface-enhanced Raman scattering (SERS) and near-infrared (NIR) absorption for imaging. Functionally, the nanochains significantly enhanced NK cell-mediated cytolysis. This result was dependent on the length of the nanochain and, notably, surpassed that of Herceptin, a clinical mAb control, because its multivalent Fc presentation facilitated stable immune synapse formation.

2 Materials and methods

2.1 Materials

Cetyltrimethylammonium bromide (CTAB, ≥99%), silver nitrate (≥99%), L-ascorbic acid (≥99%), sodium borohydride (≥98%), chloroauric acid trihydrate (≥99.9%), 4-mercaptobenzoinc acid (≥90%) and FA (≥97%) were purchased from Sigma-Aldrich (St. Louis, MO, USA). Alkyne-terminated polyethylene glycol (PEG) thiol (alkyne-PEG-SH; MW 3400 Da), azide polyethylene glycol thiol (azido-PEG-SH; MW 3400 Da), and thiol-terminated polyethylene glycol carboxylic acid (HS-PEG-COOH; MW 3500 Da) were purchased from JenKem Technology (Allen, TX, USA). Dulbecco's Modified Eagle Medium (DMEM), fetal bovine serum (FBS), and penicillin–streptomycin were purchased from Thermo Fisher Scientific (Waltham, MA, USA). Histopaque® 1077 was obtained from MilliporeSigma (Burlington, MA, USA). The IgG Fc fragment was provided by Prof. Hyojung Hong (Kangwon National University, South Korea). All solutions were prepared using Milli-Q ultrapure water (18.2 MΩ cm, Millipore).

2.2 Gold nanorod synthesis

GNRs were prepared using a seed-mediated synthesis method as described previously.[33] For the seed solution, 0.2 M CTAB (1 mL), 0.5 mM chloroauric acid (1 mL), and ice-cold 10 mM sodium borohydride 0.12 mL were mixed for 2 min. To prepare the growth solution, 4 mM silver nitrate (250 μL), 0.2 M CTAB (5 mL), 1 mM chloroauric acid trihydrate (5 mL) were gently mixed at 30 °C for 3 min; then, 78.8 mM ascorbic acid (70 μL) was added. After the yellow–brown color completely changed to a clear appearance, the seed solution (24 μL) was added. The final mixture was incubated at 30 °C for 1 h. Subsequently, the NR suspension was centrifuged at 10 000 rpm for 10 min to remove excess CTAB and then resuspended in distilled water (DW). The aspect ratio of the GNR was confirmed *via* ultraviolet-visible light spectroscopy, dynamic laser scattering (DLS), and energy-filtering transmission electron microscopy (TEM; LEO 912AB OMEGA, Carl Zeiss NTS, Jena, Germany).

2.3 Immobilization of azido and folic acid on nanorod surface

Azido-PEG-SH (50 nM) was incubated with CTAB-stabilized NR (NR_{CTAB}) solution (10 mL) for 2 h at room temperature to prepare azido-conjugated NR_{CTAB} (azidoNR_{CTAB}). Then, the mixture was centrifuged to remove unbound azido-PEG-SH. For PEG ligand exchange on the NR side, the pellet was resuspended in DW (10 mL); then, HS-PEG-COOH (10 mg mL^{-1}, 1 mL) was added to the azidoNR_{CTAB} suspension, incubated overnight, and finally centrifuged thrice at 13 500 rpm for 30 min to remove unbound PEG. To conjugate FA to the side of PEG (FA-azidoNR_{PEG}), 1-ethyl-3-(3-dimethylaminopropyl) carbodiimide (EDC) and *N*-hydroxysuccinimide (NHS) were initially reacted with azide-terminated PEG-functionalized NR (azidoNR_{PEG}) in 0.1× PBS for 30 min at room temperature; then, FA (50 μg mL^{-1}) in dimethyl sulfoxide (DMSO) was added. Alkyne-decorated NR_{CATB} (alkyneNR_{CTAB}) and alkyne-decorated NR_{PEG} (alkyneNR_{PEG}) were prepared using a similar method as that used for azidoNR_{CTAB}. To conjugate IgG Fc fragment to the side of PEG (IgG-alkyneNR_{PEG}), EDC and NHS were initially reacted with alkyneNR_{PEG} in 0.1× PBS for 30 min at room temperature; subsequently, IgG (50 μg mL^{-1}) was added. To ensure a consistent structure–function relationship analysis, the concentration of IgG was maintained at a saturation level to provide a uniform ligand density per unit surface area across all

nanorod precursors. The size distribution of IgG-alkyneNR_{PEG} was measured using DLS.

2.4 Click chemistry assembly of nanochains

To prepare the nanochains, the same particle concentrations of azidoNR_{PEG} and alkyneNR_{PEG} were mixed with 2 : 1, 3 : 2, and 4 : 3 volume ratios of azido-NR : alkyne-NR. Copper sulfate (500 μM, 0.5 mL) and ascorbic acid (10 mM, 0.5 mL) were added to the azidoNR_{PEG}/alkyneNR_{PEG} mixture for alkyne–azide cycloaddition (known as click reaction) for 6 h at room temperature. Because the nanochains were assembled from these pre-functionalized nanorod building blocks, the local density of Fc fragments and folic acid remained constant across short, medium, and long nanochains, despite the increase in total ligand count per assembly. The click reaction was also performed using azidoNR_{CTAB}/alkyneNR_{CTAB} under identical conditions. After the click reaction, the catalyst was removed by performing centrifugation thrice at 13 500 rpm for 30 min. The PEG-stabilized nanochains were characterized *via* ultraviolet-visible light spectroscopy and field-emission TEM (JEM-2100F, JEOL, Japan).

2.5 Surface-enhanced Raman scattering (SERS) analysis

The SERS intensities of the nanochains coated with 4-mercaptobenzoinc acid (4-MBA) were compared according to the chain length. To decorate the GNR surfaces with Raman reporter dye, the NR suspension (0.2 nM, 500 μL) was centrifuged down and the pellet was resuspended in DW (50 μL). Subsequently, 4-MBA (0.5 mM, 200 μL) in ethanol and PEG (10 mg mL^{-1}, 50 μL) in DW were added to the concentrated NR suspension, followed by the sequential addition of citrate in DMSO (100 mM, 300 μL); this was incubated for 30 min, followed by the addition of ethanol (400 μL). After further incubation for 1 h, the NRs were washed with ethanol *via* centrifugation, and the purified NRs were end-to-end assembled following the aforementioned conditions. The nanochain suspension in ethanol was characterized using Raman spectroscopy. The SERS spectra were obtained using a Jobin Yvon/HORIBA LabRam HR Evolution Raman spectrometer with integral BX41 and BXFM confocal microscopes at Kangwon Radiation Convergence Research Suppor Center of Korra Basic Science Institute (KBSI) in Kangwon National University. An air-cooled intracavity-regulated 785 nm laser was used as the excitation source. Raman scattering was detected at a 180° geometry using a multichannel air-cooled (−60 °C) charge-coupled device camera (1024 × 256 pixels). The Raman shift was calibrated using a Si wafer, which has a characteristic Raman shift at 520 cm^{-1}. All Raman spectra were collected after a 5 s exposure time and two accumulations with a 600 gr per mm grating.

2.6 Cell culture and immune cell isolation

KB cell (ATCC #CRL-3596, Manassas, VA), a human oral cancer cell line and subline of HeLa cell, was maintained in 10% FBS-supplemented DMEM in 5% CO_2 under a humidified condition at 37 °C. Peripheral blood mononuclear cells (PBMCs) were isolated from the whole blood sample of a single human donor (African American Male, age: 41 years (Innovative™ Research, MI)). All ADCC assays were performed using three independent replicates ($n = 3$) with effector-to-target ratios carefully controlled at 5 : 1. The whole blood (3 mL) was blended with pre-warmed PBS (10 mL) and layered on top of pre-warmed Histopaque® 1077 (3 mL) at 25 °C. After centrifugation at 400×*g* for 30 min, the upper layer was carefully removed, and the remaining intermediate opaque layer containing mononuclear cells was transferred to a new plastic tube and washed twice with fresh PBS (10 mL) by centrifugation at 250×*g* for 10 min. Finally, the purified PBMCs were suspended in isolation buffer (500 μL; PBS with 2% FBS and 2 mM EDTA). To isolate NK cells from the isolated PBMCs, $CD16^+$ cells were obtained using the Dynabead™ Unthouched™ Human NK Cell Kit (Thermo Fisher Scientific, IN) according to the protocols specified by the manufacturer. Briefly, PBMC suspension (500 μL) was mixed with FBS (100 μL) and the antibody cocktail (100 μL), incubated for 20 min at 4 °C, and treated with Dynabeads for 15 min. The antibody-coated cells were eliminated using a magnet, and the uncoated $CD16^+$ cells in the supernatants were harvested for further study.

2.7 SERS mapping of KB cells

The surface of the nanochain decorated with 30 μg of 4-MBA-treated KB cells was observed using Raman scattering. KB cells on cover slips were incubated with the nanochain in 10% FBS-supplemented DMEM at 37 °C for 3 h. The incubated cells were fixed in 4% formaldehyde for 15 min and analyzed *via* Raman spectroscopy using a 785 nm laser for 10 s. For the mapping analysis of KB cells, a Raman signal between 1050–1150 cm^{-1} was employed.

2.8 Folic acid receptor-mediated nanochain targeting

To characterize the targeting ability of the nanochains toward FA receptors, KB cells were treated with different amounts of nanochains with and without FA in the culture medium. For blocking FA receptors on KB cells, KB cells (5×10^4 cells) were pre-incubated in 1 mM FA for 1 h. KB cells were incubated with 0.2 nM of nanochains for 3 h and then treated with 0.5 mL of aqua regia to completely dissolve the gold in the cells. After diluting the mixture with DW, the gold concentration was quantified using inductively coupled plasma optical emission spectrometry (Optima 7300 DV, PerkinElmer) at the Central Laboratory of Kangwon National University. Cellular uptake was calculated using the following equation:

$$\text{Cellular uptake}(\%) = \left(\frac{\text{gold content in cells}}{\text{initial amount of gold treated to cell}}\right) \times 100$$

2.9 Nanochain-mediated antibody-dependent cellular cytotoxicity analysis

Nanochain-mediated ADCC effect was evaluated *via* the cell lysis rate using the Delfia® EuTDA Cytotoxicity reagent (PerkinElmer Live Sciences, Norwalk, CT). Following the protocols

specified by the manufacturer with minor modifications, KB cells on a 24-well plate were pre-incubated with nanochains (0.2 nM) for 3 h and the medium was replaced with fresh DMEM. For a positive control, KB cells pretreated with Herceptin (5 μg mL^{-1}) were prepared. The nanochain-treated KB cells were stained with the Delfia BATDA reagent (0.5 μL mL^{-1} of PBS) in 2% FBS-supplemented DMEM for 20 min at 37 °C. Subsequently, the cells were washed twice, and treated with $CD16^{+}$-enriched PBMCs at a five-fold ratio to KB cells, and incubated at 37 °C for 4 h. The supernatant (20 μL) was mixed with Europium solution (200 μL) and gently mixed for 15 min, and the fluorescence was measured using a time-resolved fluorometer (excitation/emission: 337 nm/615 nm). The released TDA was converted into a specific cell lysis rate using the following equation:

$$\text{Specific cell lysis rate}(\%) = \frac{\text{experimental release} - \text{spontaneous release}}{\text{maximum release} - \text{spontaneous release}} \times 100$$

Moreover, $CD16^{+}$-enriched PBMCs were pretreated with the Human TruStain FcX™ (BioLegend, San Diego, CA, USA) blocking buffer to confirm the Fc-receptor-mediated cell lysis rate. The reagent (25 μL) was mixed with PBMCs (1 mL) and incubated on ice for 5 min. Then, the cells were incubated with nanochain-coated KB cells, and the cell lysis rate was quantified using the method described above.

2.10 Statistical analysis

Statistical analysis was performed using a Student's *t*-test or one-way ANOVA in the software SigmaPlot version 14.0 with $n = 3$; error bars indicate standard deviation, unless indicated otherwise, and *p*-values <0.05 were considered statistically significant.

3 Results and discussion

3.1 End-to-end assembly of targeted and immune-activating nanochains

Nanowire- and nanochain-based delivery systems enhance multivalent receptor interactions and tumor accumulation, which is consistent with the increased ADCC efficiency observed with longer nanochains. Their modular architecture spatially

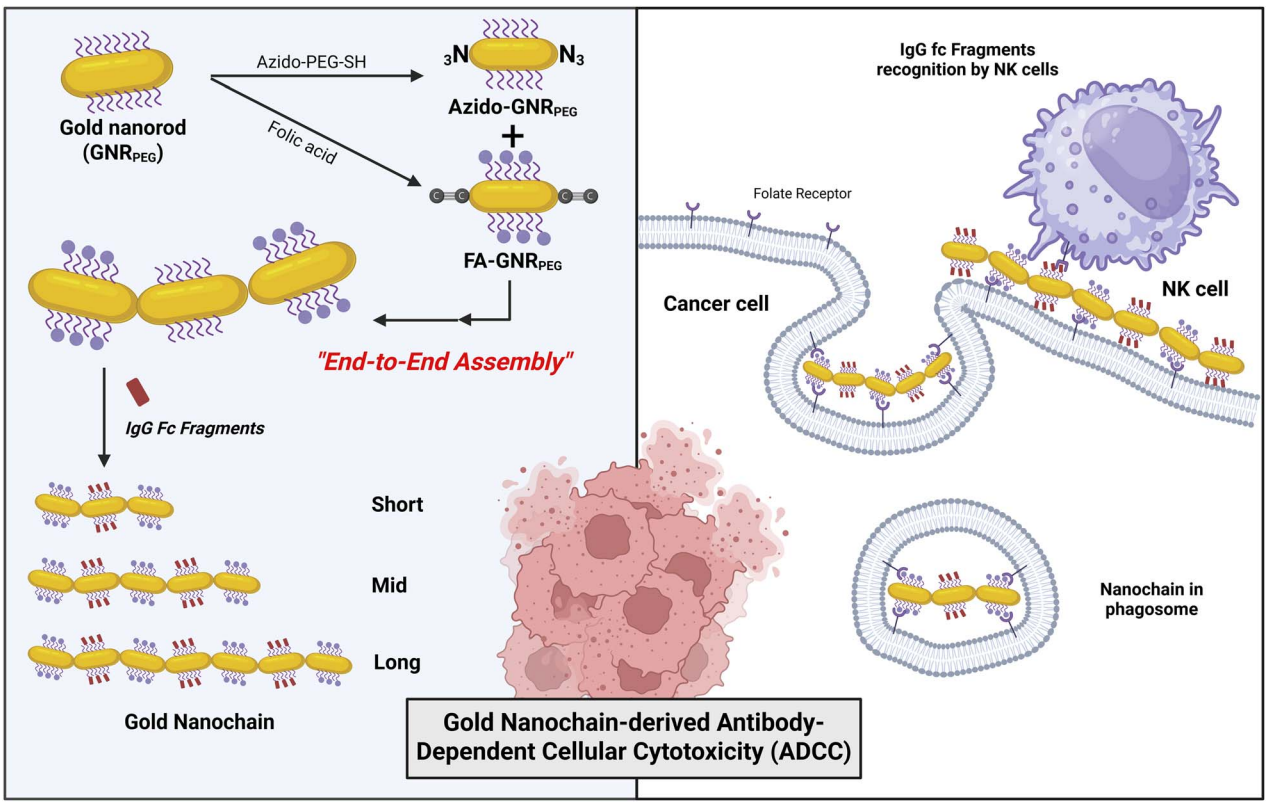

Fig. 1 Schematic illustration of the preparation and length-tunable assembly of gold nanochains for enhanced antibody-dependent cellular cytotoxicity (ADCC). Gold nanorods (GNR$_{PEG}$) were functionalized with azido-PEG-SH and folic acid to produce azido- and folate-modified nanorods (azido-GNR$_{PEG}$ and FA-GNR$_{PEG}$). These nanorods were assembled end-to-end *via* a click chemistry reaction to form nanochains with lengths controlled by stoichiometric ratios, where short chains ($n = 2 \approx 3$ rods) *via* a 2 : 1 ratio.; medium chains ($n = 5 \approx 7$ rods) *via* a 3 : 2 ratio; long chains ($n > 7$ rods) *via* a 4 : 3 ratio. The "linear-scaffold" architecture of the long nanochain (approx. 7 rods) was identified as the optimal design for promoting potent ADCC through enhanced immune synapse formation. The nanochains were further conjugated with IgG Fc fragments, providing bimodal surface functionalities with folate and Fc domains. Upon binding to folate receptor-overexpressing cancer cells, these Fc-modified nanochains engage NK cells through Fc receptor recognition, thereby promoting potent antibody-dependent cellular cytotoxicity (ADCC) against cancer cells.

separates the targeting ligands from the Fc units, minimizing steric hindrance and promoting efficient NK cell activation. Moreover, plasmonic coupling and flexible linkers provide tunable photothermal/SERS properties and sustained receptor clustering, highlighting nanochains as promising platforms for advanced antibody-dependent cancer therapy.

Fig. 1 illustrates the stepwise "end-to-end" assembly of GNRs into nanochains through click chemistry between azido- and alkyne-functionalized GNRs. The termini of the GNRs were selectively modified with azido- or alkyne-PEG-SH ligands, whereas the lateral surfaces were functionalized with carboxylate groups *via* ligand exchange. Because of the facet-selective binding of CTAB, thiolated ligands preferentially attach to the rod ends, enabling site-specific conjugation by adjusting the ligand concentration.[34,35] An optimal azido/alkyne-PEG-SH concentration (50 nM) promoted efficient end-to-end linkage. Prior to assembly, FA was conjugated to the carboxylated sides of the alkyne-GNRs (FA-GNR$_{PEG}$), whereas azido-GNR$_{PEG}$ maintained the reactive termini. Mixing these two types of NRs in controlled ratios (2 : 1, 3 : 2, and 4 : 3) yielded short, medium, and long nanochains, respectively. The resulting folate-decorated nanochains were subsequently functionalized with IgG Fc fragments to enable immune cell engagement. Folate serves as a stable low-immunogenicity targeting ligand that mediates receptor-specific uptake, whereas the Fc regions recruit NK cells to induce ADCC. This modular configuration facilitates the spatial separation of targeting and immune-activating units, integrating tumor recognition and immune stimulation into a single theranostic nanochain platform. Subsequent conjugation of the IgG Fc fragments to the remaining carboxylate groups yielded nanochains composed of alternating folate- and Fc-functionalized NRs. Because each NR was pre-functionalized before assembly, different ligands could be selectively positioned along the nanochain, enabling the integration of targeting, therapeutic, or immune-modulating functions within a single structure. The anisotropic chain-like geometry provides a larger contact interface with the cancer cell membrane than spherical nanoparticles, facilitating multivalent folate–receptor interactions and enhancing cellular uptake.[21,36,37] Meanwhile, the exposed Fc fragments on the nanochain surface effectively engaged NK cells, promoting ADCC. The flexible PEG linkers between the NRs allowed adaptive conformations on the membrane surface, maintaining receptor clustering and efficient immune activation. Therefore, we speculate that this modular and dynamic architecture supports both tumor-specific targeting and NK cell-mediated immune responses.

3.2 Characteristics of gold nanorods and nanochains

The characteristics of NRs and nanochains are shown in Fig. 2. Because NRs possess an anisotropic structure, the hydrodynamic size distribution of NR$_{CTAB}$ displayed a bimodal profile (Fig. 2A). After PEG ligand exchange, the size distribution shifted toward larger diameters, confirming successful PEG decoration on the nanorod surface (NR$_{PEG}$). UV-visible absorption spectra revealed the characteristic plasmon bands of NR$_{CTAB}$ at

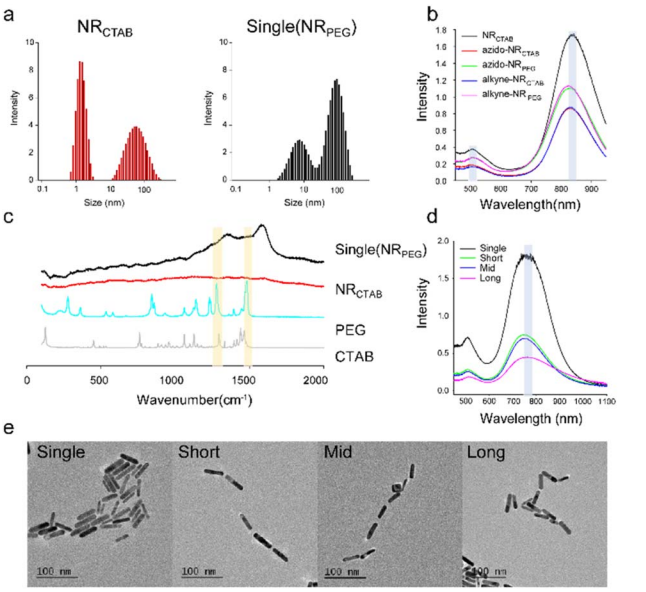

Fig. 2 Physicochemical characterization of gold nanorods and nanochains. (a) Size distribution profiles of CTAB-stabilized nanorods (NR$_{CTAB}$) and PEG ligand-exchanged nanorods (NR$_{PEG}$), revealing a bimodal distribution for CTAB-stabilized rods due to their anisotropy. (b) UV-visible spectra of NR$_{CTAB}$ and NR$_{PEG}$, with transverse and longitudinal plasmon peaks indicated by dashed green lines, demonstrating red-shifting upon PEG modification. (c) FTIR spectra confirming PEG immobilization, where characteristic PEG vibrational peaks shifted upon ligand exchange (highlighted with yellow boxes). (d) UV-visible spectral changes following click-mediated nanochain formation, demonstrating plasmonic coupling between assembled nanorods. (e) Transmission electron microscopy (TEM) image confirming end-to-end assembly into elongated nanochain structures.

~510 nm (transverse) and ~830 nm (longitudinal) (Fig. 2B). Quantitative spectral analysis confirmed the successful surface modification and subsequent assembly of the nanostructures. The initial ligand exchange to PEG on the nanorod surface (NR$_{PEG}$) resulted in a measurable redshift of the localizaed surface plasmon resonance (LSPR) peak from 830 nm to 834 nm ($\Delta\lambda$ = 4 nm). Following the click-mediated assembly into nanochains, the intensity of the longitudinal peak decreased, while NIR absorbance increased, with a characteristic peak shift to ~845 nm, confirming successful end-to-end plasmonic coupling between the constituent rods. PEG grafting was further confirmed using Fourier transform infrared spectroscopy (Fig. 2C). As PEG was immobilized on the NR surface, the characteristic C–H and C–O–C stretching bands at 2880 and 1100 cm^{-1} shifted to ~2870 and ~1115 cm^{-1}, respectively, indicating successful surface binding of PEG chains. After the click reaction, the optical features of the nanochains revealed an end-to-end assembly behavior. The intensity of the longitudinal plasmon peak decreased, whereas the absorbance in the NIR region increased (Fig. 2D). These spectral changes occurred because the assembled NRs behaved as coupled plasmonic entities rather than as isolated particles. Previous studies have shown that side-by-side assembly induces a blue shift in the longitudinal band, whereas end-to-end assembly leads to a red

shift owing to plasmon coupling along the rod axis.[38–40] However, in our case, no distinct red shift was observed. We speculate that this was due to the flexible PEG linkers (MW 3500) conjugated at the rod termini, where the ends of the NR were connected *via* polymer spacers after the click reaction, producing chain-like assemblies that extended into the NIR region but may not have coupled strongly enough to generate a clear red shift, as seen in rigid assemblies. The polymer chain flexibility plays a critical role in determining the plasmonic response of the assembled nanostructures. While hydrophobic polymers such as polystyrene have been used as rigid linkers to drive assembly *via* strong hydrophobic interactions, PEG in aqueous solutions possesses significantly higher conformational flexibility, which may dampen plasmon coupling effects.[41,42] Thus, although PEG facilitates biocompatibility and modular assembly, its dynamic nature in water may reduce plasmon resonance shifts. Finally, the morphology of the nanochains was confirmed *via* TEM (Fig. 2E), which clearly showed end-to-end linked NRs. Furthermore, the nanochain length could be modulated by varying the NR mixing ratio during the click reaction, producing short, medium, and long assemblies. This tunability enables the precise control of structural dimensions for biomedical applications, particularly those requiring the optimization of plasmonic properties and biological interactions.

3.3 SERS signals of gold nanochain

The assembled nanochain structure was further validated through modulation of SERS signals, in Fig. 3. To impart Raman sensitivity, the NRs were co-decorated with the Raman reporter dye, 4-MBA, along with PEG ligands and subsequently induced to form end-to-end nanochains. The SERS spectra clearly showed a marked reduction in the characteristic Raman bands of 4-MBA at 1078 and 1590 cm^{-1} under equivalent gold concentrations, correlating with nanochain elongation, as shown in Fig. 3A. This modulation of SERS intensity is primarily governed by the interparticle gap, which dictates the strength of localized electromagnetic "hot spots" that are responsible for Raman enhancement.[43] Previous reports demonstrated that ultrashort interparticle spacings (<2 nm) in silver or gold nanoparticle assemblies yield significantly strong SERS activity, owing to intense field confinement at nanogaps.[44] Similarly, engineered GNR assemblies have been exploited to generate plasmonic junctions for high-sensitivity molecular detection, offering a versatile platform for biomedical imaging and diagnostics.[45] Particularly, Zhu and colleagues showed that NRs can be designed to self-assemble in the presence of specific toxins, thereby triggering strong Raman outputs; their computational modeling further revealed that end-to-end assemblies with ~15 nm gaps can substantially amplify the electric field intensity at the junctions, which directly coincides with SERS signal enhancement.[46] However, the proposed system exhibited a relative decrease in SERS intensity when nanochains were bridged *via* two PEG linkers, which likely increased the interparticle gap beyond the optimal range for hot-spot generation. This phenomenon is consistent with theoretical and

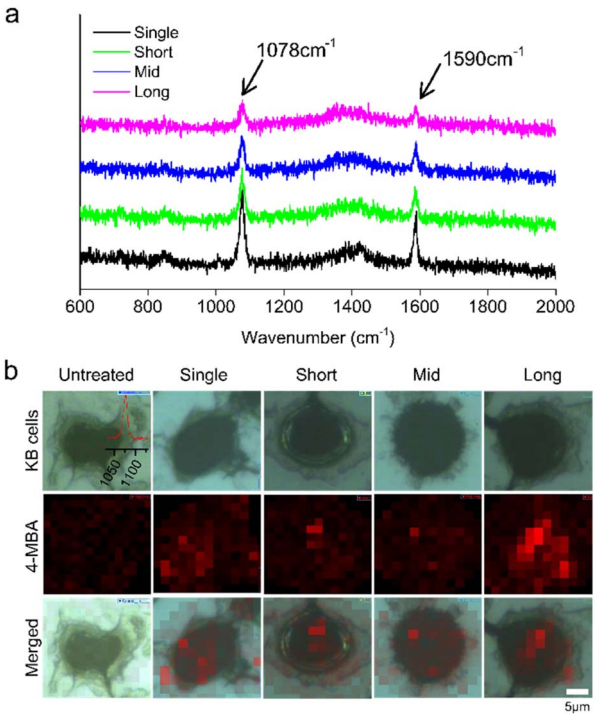

Fig. 3 Surface-enhanced Raman scattering (SERS) properties of gold nanochains in aqueous solution *versus* intracellular environments. (a) Raman spectra of aqueous suspensions of nanochains functionalized with the Raman reporter dye 4-mercaptobenzoic acid (4-MBA). Spectra are compared across single nanorods (control) and nanochains of increasing length. A progressive reduction in the intensity of characteristic 4-MBA peaks (1078 cm^{-1} and 1590 cm^{-1}) is observed with increased elongation, attributed to the relatively large interparticle spacing in the linear configuration which limits electromagnetic enhancement. (b) SERS mapping of KB cells (folate receptor-positive) following incubation with nanochains or single nanorods (0.5 μm step size; scale bar = 5 μm). While single nanorods produce weak and evenly distributed signals, nanochain-treated cells exhibit discrete, high-intensity Raman "hot spots". These hot spots in long nanochains arise from intracellular folding within endosomes, bringing non-adjacent nanorods into close proximity (<10 nm) to create 3D plasmonic hotspots that significantly amplify the SERS signal compared to the rigid linear or single-rod states.

experimental studies showing that SERS enhancement decays exponentially with increasing interparticle distance.[47] Moreover, the aspect ratio of an NR strongly influences the plasmonic resonance; shorter NRs couple more efficiently with excitation sources, thereby producing stronger electromagnetic enhancement, whereas elongated NRs result in red-shifted plasmon modes and weaker SERS output.[48,49] Collectively, these observations indicate that the attenuated SERS response in our system provides indirect but compelling evidence that the NRs underwent end-to-end PEG-mediated assembly, thereby forming nanochains, as shown in Fig. 3.

We further investigated the potential of the nanochains for cellular SERS imaging, which revealed a striking length-dependent behavior (Fig. 3B). KB cells were incubated with single NRs, short, medium, and long nanochains for 3 h. While single NRs and short nanochains ($n \approx 2$–3) produced relatively weak and evenly distributed Raman signals across the

cytoplasm, the long nanochains generated highly localized and intense "hot spots". This reuslt suggests a fundamental difference in structural adaptation within the cellular environment. Unlike the rigid single rods or short assemblies that remain dispersed, long nanochains possess greater conformational flexibility, allowing them to undergo intracellular folding within endosomes. This folding brings non-adjacent nanorods into close proximity (<10 nm), creating 3D plasmonic hotspots that are absent in shorter, more linear structures. Thus, the intense localized signals observed in the long nanochain group serve as evidence of their unique ability to form high-density electromagnetic fields upon cellular internalization. Note that all groups were compared under conditions normalized to the same total gold concentration, ensuring that the observed differences arose from the assembly state and length-dependent structural folding rather than the overall probe amount.

3.4 Length-dependent immunotherapeutic efficacy of multi-chained nanorods

To further evaluate ligand-mediated targeting, FA functionalization was employed, exploiting the overexpression of folate receptors in KB cells. Quantification of cell membrane binding and intracellular uptake revealed comparable efficiencies between single NRs and nanochains when normalized to similar total gold inputs (Fig. 4). However, pretreatment of KB cells with excess free FA significantly reduced the cellular association of both single and assembled nanostructures, thereby confirming that the observed binding was predominantly mediated by FA–receptor interactions rather than nonspecific uptake. Therefore, these findings indicate that nanochains retain the targeting capacity of their folate ligands while exhibiting unique spatial clustering behavior inside cells, making them promising candidates for localized SERS imaging applications.

Subsequently, the immunotherapeutic potential of multi-ligand unit-decorated nanochains was explored, which can act as modular linkers between different cell types. A previous study demonstrated that site-specific decoration of distinct ligands on gold/nickel electrodeposited NRs enabled simultaneous targeting of dendritic cells and T lymphocytes, thereby facilitating immune synapse formation.[50] Extending this concept, we investigated the cytolytic effect of KB cells that were pretreated with nanochains of varying lengths when co-cultured with $CD16^{+}$ effector cells. In this study, single nanorods were selected as the primary control to isolate the specific impact of assembly length and anisotropy while maintaining a consistent chemical building block across all groups.

As shown in Fig. 4, the percentage of KB cell lysis is strongly dependent on the chain length, with seven-rod nanochains inducing the highest cytolysis compared to that of the three- and five-rod assemblies. Notably, the cytolytic activity of the seven-rod nanochains surpassed that of Herceptin, which was used as the positive control. In contrast, single NRs produced only ~30% lysis, underscoring the functional superiority of the multichain architectures. Mechanistically, we speculated that the linear linkage of NRs altered their cell membrane

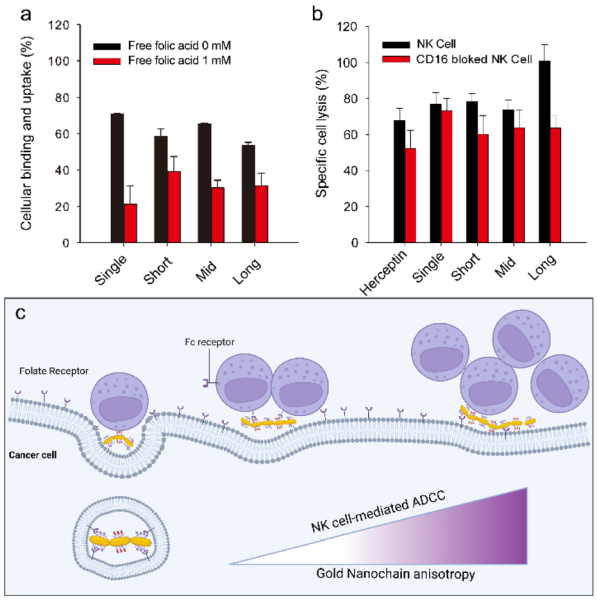

Fig. 4 Mechanism of nanochain-mediated ADCC. (a) ICP-OES quantification showed efficient binding and internalization of nanochains in KB cells, while pre-treatment with excess free folic acid (1 mM) competitively inhibited uptake, confirming folate receptor-mediated targeting. (b) When PBMCs were pre-incubated with an anti-CD16 antibody, nanochain-induced lysis of KB cells was significantly reduced, demonstrating that cytotoxicity relies on Fc–CD16 interactions. In europium-TDA assays using an effector-to-target ratio of 10 : 1, nanochain-mediated cytotoxicity increased with chain length, with seven-rod assemblies exhibiting markedly higher lysis than three- or five-rod nanochains and surpassing the activity of Herceptin (positive control). (c) The proposed mechanism involves the selective binding of folate/IgG Fc-decorated nanochains to tumour cells *via* overexpressed folate receptors, followed by recognition of the Fc fragments by CD16 receptors on NK cells to trigger ADCC. Longer nanochains persist on the tumour cell membrane for extended periods, providing higher Fc presentation density and enhancing NK cell engagement. The linear and flexible PEG-linked architecture further promotes receptor clustering and boosts cytotoxic efficacy.

interactions and persistence. Although single NRs were rapidly internalized and cleared from the membrane within 2 h, longer chains were more difficult to eliminate, leading to prolonged exposure of the surface ligands. This is critical because the antibody fragment (Fc) density and spatial orientation on the membrane directly influence immune cell recognition. Moreover, the PEG linkers between the rods confer structural flexibility, enabling nanochains to dynamically adapt their conformation and maximize multivalent interactions at immune synapses.

Together, these features contribute to enhanced recruitment of effector cells and cytotoxicity. Conventional nanoparticle-based antibody delivery systems generally rely on entire antibodies, where the fragment antigen-binding (Fab) region binds to tumor antigens and Fc region simultaneously engages immune effector cells. However, the random orientation of antibodies on spherical nanoparticles limits Fc accessibility and reduces immune engagement.[51,52] Antibody fragment-based approaches partially overcome this by allowing Fab fragments

to be preferentially oriented outward; however, they still suffer from geometric constraints that are imposed by spherical architectures. In contrast, the multi-chained NR strategy provides a linear anisotropic scaffold in which Fc fragments can be presented in a more controlled and repetitive fashion along the chain axis. Recent topological studies on artificial immunological interfaces confirm that elongated or tubular morphologies better activate immune cells compared to spherical counterparts, particularly by providing a more stable and biomimetic interface for receptor clustering and synapse formation.[53] Supporting evidence from other nanoparticle systems highlighted the importance of these design principles. For example, CD20-targeted silver nanoparticles and SERS dye-decorated nanoparticles enhance ADCC and enable multiplexed lymphoma cell detection, while multivalent presentation of trastuzumab half-chains on iron oxide nanoparticles further amplifies antitumor efficacy and overcomes resistance in HER2-positive cells by strengthening ADCC.[54] Similarly, SERS dye-decorated nanoparticles facilitated the multiplexed detection of lymphoma cells while maintaining immunotherapeutic efficacy. Trastuzumab-loaded poly(D,L-lactide-*co*-glycolic acid) nanoparticles have also been reported to target tumor cells, although their therapeutic efficiency was partly limited by antibody release during polymer degradation.[55] Also, lipid nanoparticle (LNP) platforms demonstrate that delivering immune-boosting factors like CD70 mRNA alongside tumor antigens can significantly enhance ADCC and NK cell activity, providing a robust strategy for next-generation immunotherapy.[56]

Compared to these spherical systems, our multi-chained NR platform offers distinct advantages: (i) controlled antibody fragment orientation, (ii) flexible yet persistent membrane engagement, (iii) stronger Fc-immune receptor clustering, and (iv) the potential to integrate diagnostic SERS signals for theranostic applications. In summary, this study provides a robust *in vitro* proof-of-concept for the theranostic potential of the multi-chained NR platform, bridging the gap between high-sensitivity SERS imaging and potent antibody-dependent cellular cytotoxicity. While these findings demonstrate superior immune cell recruitment and cytotoxicity, we acknowledge that the current evaluation is limited to controlled laboratory environments. Consequently, further investigations are required to translate these findings into clinical settings. Future work will specifically focus on evaluating the *in vivo* pharmacokinetics, biodistribution, and long-term therapeutic efficacy of these nanochains in complex physiological environments to fully validate their potential as next-generation immunotheranostics.

4 Conclusions

This study introduced a nanochain platform that combines the benefits of anisotropic nanostructures, modular ligand decoration, and precise chemical assembly to potentiate antibody-dependent cancer immunotherapy. The nanochains demonstrated prolonged retention on tumor cell membranes, enhanced accessibility of Fc fragments for NK cell engagement, and tunable photonic properties that are suitable for imaging and theragnostic applications. Importantly, the ability to spatially separate tumor-targeting moieties from immune-activating Fc domains addresses a longstanding challenge in nanomedicine, that is, the orientation control of antibodies and fragments. The modularity of the nanochain systems offers numerous opportunities for translation. Furthermore, their intrinsic SERS and photothermal properties make them attractive candidates for image-guided therapy and combinatorial regimens. While the current results demonstrate a robust *in vitro* proof-of-concept for the theranostic potential of gold nanochains, we acknowledge that testing across a broader range of cancer cell lines, such as SKOV-3 or HeLa, and *in vivo* pharmacokinetics studies are essential next steps for clinical translation. To ensure platform generalizability, upcoming evaluations will address donor-to-donor variability in NK cell responses. Furthermore, we aim to establish translational feasibility by conducting *in vivo* pharmacokinetics and immunogenicity assessments, alongside comparative trials with established antibody-drug conjugates (ADCs). Collectively, these findings suggest that nanochains are versatile and powerful next-generation platforms for synergistic cancer immunotherapy.

Author contributions

Chungmo Yang: data curation, validation, visualization, investigation, writing – original draft, and writing – review & editing. Young Ju Son: conceptualization, investigation, methodology, data curation, and writing – original draft. Sila Jin: data curation, methodology, and validation. Yeonju Park: data curation, writing – review & editing, Young Mee Jung: supervision, funding acquisition and validation. Seung Goo Kang: supervision, funding acquisition and validation. Hyuk Sang Yoo: conceptualization, supervision, funding acquisition, validation, writing – original draft, and writing – review & editing.

Conflicts of interest

There are no conflicts to declare.

Data availability

The data that support the findings of this study are available upon reasonable request from the authors.

Acknowledgements

This work was supported by a grant from Ministry of Science and ICT (RS-2025-02073096; RS-2024-00339160) and a grant from the Ministry of Education (RS-2023-00271205).

References

1 S. Pinto, J. Pahl, A. Schottelius, P. J. Carter and J. Koch, *Trends Immunol.*, 2022, **43**, 932–946.

2 W. Wang, A. K. Erbe, J. A. Hank, Z. S. Morris and P. M. Sondel, *Front. Immunol.*, 2015, 6.
3 J. Kurai, H. Chikumi, K. Hashimoto, K. Yamaguchi, A. Yamasaki, T. Sako, H. Touge, H. Makino, M. Takata, M. Miyata, M. Nakamoto, N. Burioka and E. Shimizu, *Clin. Cancer Res.*, 2007, **13**, 1552–1561.
4 M. Xiao, Q. Tang, S. Zeng, Q. Yang, X. Yang, X. Tong, G. Zhu, L. Lei and S. Li, *Biomater. Res.*, 2023, **27**, 47.
5 T. R. Serna-Gallegos, C. J. La-Fargue and K. S. Tewari, *Recent Pat. Biotechnol.*, 2018, **12**, 101–112.
6 L. P. Díaz, S. Millán, N. Chaban, A. d. Campo and E. Spitzer, *Future Oncol.*, 2021, **17**, 2529–2544.
7 A. Lin, P. Ye, Z. Li, A. Jiang, Z. Liu, Q. Cheng, J. Zhang and P. Luo, *Research*, 2025, **8**, 0723.
8 A. M. Scott, J. D. Wolchok and L. J. Old, *Nat. Rev. Cancer*, 2012, **12**, 278–287.
9 L. M. Weiner, R. Surana and S. Wang, *Nat. Rev. Immunol.*, 2010, **10**, 317–327.
10 M. C. Ochoa, L. Minute, I. Rodriguez, S. Garasa, E. Perez-Ruiz, S. Inogés, I. Melero and P. Berraondo, *Immunol. Cell Biol.*, 2017, **95**, 347–355.
11 C. L. Nigro, M. Macagno, D. Sangiolo, L. Bertolaccini, M. Aglietta and M. C. Merlano, *Ann. Transl. Med.*, 2019, **7**, 105.
12 M. Ahmed, D. W. Pan and M. E. Davis, *Bioconjugate Chem.*, 2015, **26**, 812–816.
13 S. Centi, F. Tatini, F. Ratto, A. Gnerucci, R. Mercatelli, G. Romano, I. Landini, S. Nobili, A. Ravalli, G. Marrazza, E. Mini, F. Fusi and R. Pini, *J. Nanobiotechnol.*, 2014, **12**, 55.
14 C. Parolo, A. de la Escosura-Muñiz, E. Polo, V. Grazú, J. M. de la Fuente and A. Merkoçi, *ACS Appl. Mater. Interfaces*, 2013, **5**, 10753–10759.
15 B. Saha, P. Songe, T. H. Evers and M. W. J. Prins, *Analyst*, 2017, **142**, 4247–4256.
16 A. Jain, Q. Zhang and H.-C. Toh, *Chin. J. Cancer*, 2017, **36**, 67.
17 D. Chenthamara, S. Subramaniam, S. G. Ramakrishnan, S. Krishnaswamy, M. M. Essa, F.-H. Lin and M. W. Qoronfleh, *Biomater. Res.*, 2019, **23**, 20.
18 Z. Hua, J. R. Jones, M. Thomas, M. C. Arno, A. Souslov, T. R. Wilks and R. K. O'Reilly, *Nat. Commun.*, 2019, **10**, 5406.
19 S. Barua, J.-W. Yoo, P. Kolhar, A. Wakankar, Y. R. Gokarn and S. Mitragotri, *Proc. Natl. Acad. Sci. U. S. A.*, 2013, **110**, 3270–3275.
20 R. Toy, P. M. Peiris, K. B. Ghaghada and E. Karathanasis, *Nanomedicine*, 2014, **9**, 121–134.
21 Y. Geng, P. Dalhaimer, S. Cai, R. Tsai, M. Tewari, T. Minko and D. E. Discher, *Nat. Nanotechnol.*, 2007, **2**, 249–255.
22 S. Nejati, E. Mohseni Vadeghani, S. Khorshidi and A. Karkhaneh, *Eur. Polym. J.*, 2020, **122**, 109353.
23 X. Kang, D. Li and R. Sun, *Front. Clin. Med.*, 2025, 12.
24 E. Blanco, H. Shen and M. Ferrari, *Nat. Biotechnol.*, 2015, **33**, 941–951.
25 H. Meng and A. E. Nel, *Adv. Drug Delivery Rev.*, 2018, **130**, 50–57.
26 H. J. van der Horst and T. Mutis, *Immunol. Rev.*, 2024, **328**, 456–465.
27 D. Chen, Y. Zhao, M. Li, H. Shang, N. Li, F. Li, W. Wang, Y. Wang, R. Jin, S. Liu, X. Li, S. Gao, Y. Tian, R. Li, H. Li, Y. Zhang, M. Du, Y. Cao, Y. Zhang, X. Li, Y. Huang, L. A. Hu, F. Li and H. Zhang, *Theranostics*, 2021, **11**, 1901–1917.
28 J. Kim, B. J. Lee, S. Moon, H. Lee, J. Lee, B.-S. Kim, K. Jung, H. Seo and Y. Chung, *Biomater. Res.*, 2024, **28**, 0080.
29 X. Yu, J. Zhou, H. Liang, Z. Jiang and L. Wu, *Prog. Mater. Sci.*, 2018, **94**, 114–173.
30 C. Shuai, X. Chen, C. He, G. Qian, Y. Shuai, S. Peng, Y. Deng and W. Yang, *Biomater. Res.*, 2022, **26**, 38.
31 Z. Ji, X. Wang, H. Zhang, S. Lin, H. Meng, B. Sun, S. George, T. Xia, A. E. Nel and J. I. Zink, *ACS Nano*, 2012, **6**, 5366–5380.
32 Z. Nie, D. Fava, E. Kumacheva, S. Zou, G. C. Walker and M. Rubinstein, *Nat. Mater.*, 2007, **6**, 609–614.
33 D. K. Smith and B. A. Korgel, *Langmuir*, 2008, **24**, 644–649.
34 S. Amatori, A. Lopez, C. Meneghini, A. Calcabrini, M. Colone, A. Stringaro, S. Migani, I. Khalakhan, G. Iucci, I. Venditti and C. Battocchio, *Nanoscale Adv.*, 2023, **5**, 3924–3933.
35 Y. Bao and A. Oluwafemi, *Chem. Commun.*, 2024, **60**, 469–481.
36 W. Zhang, R. Taheri-Ledari, F. Ganjali, S. S. Mirmohammadi, F. S. Qazi, M. Saeidirad, A. KashtiAray, S. Zarei-Shokat, Y. Tian and A. Maleki, *RSC Adv.*, 2023, **13**, 80–114.
37 A. Sohrabi Kashani and M. Packirisamy, *Int. J. Mol. Sci.*, 2021, **22**, 9587.
38 P. Chapagain and S. Neupane, in *Optoelectronics - Recent Advances*, ed. T. Para, IntechOpen, London, 2023, DOI: 10.5772/intechopen.1002702.
39 A. K. Sahu and S. Raj, *Gold Bull.*, 2022, **55**, 19–29.
40 P. K. Jain, S. Eustis and M. A. El-Sayed, *J. Phys. Chem. B*, 2006, **110**, 18243–18253.
41 J. Tian, F. Zheng, Q. Duan and H. Zhao, *J. Mater. Chem.*, 2011, **21**, 16928–16934.
42 J. Song, P. Huang and X. Chen, *Nat. Protoc.*, 2016, **11**, 2287–2299.
43 G. Braun, I. Pavel, A. R. Morrill, D. S. Seferos, G. C. Bazan, N. O. Reich and M. Moskovits, *J. Am. Chem. Soc.*, 2007, **129**, 7760–7761.
44 C. Lin, Y. Li, Y. Peng, S. Zhao, M. Xu, L. Zhang, Z. Huang, J. Shi and Y. Yang, *J. Nanobiotechnol.*, 2023, **21**, 149.
45 S. Nie and S. R. Emory, *Science*, 1997, **275**, 1102–1106.
46 Y. Zhu, H. Kuang, L. Xu, W. Ma, C. Peng, Y. Hua, L. Wang and C. Xu, *J. Mater. Chem.*, 2012, **22**, 2387–2391.
47 M. Moskovits, *Rev. Mod. Phys.*, 1985, **57**, 783–826.
48 S. Yun, M. K. Oh, S. K. Kim and S. Park, *J. Phys. Chem. C*, 2009, **113**, 13551–13557.
49 K. Park, L. F. Drummy, R. C. Wadams, H. Koerner, D. Nepal, L. Fabris and R. A. Vaia, *Chem. Mater.*, 2013, **25**, 555–563.
50 Y. J. Son, H. Kim, K. W. Leong and H. S. Yoo, *ACS Nano*, 2013, **7**, 9771–9779.
51 D. A. Richards, A. Maruani and V. Chudasama, *Chem. Sci.*, 2017, **8**, 63–77.
52 N. K. Lee, S.-N. Kim and C. G. Park, *Biomater. Res.*, 2021, **25**, 44.

53 A. C. Wauters, J. F. Scheerstra, I. G. Vermeijlen, R. Hammink, M. Schluck, L. Woythe, H. Wu, L. Albertazzi, C. G. Figdor, J. Tel, L. K. E. A. Abdelmohsen and J. C. M. van Hest, *ACS Nano*, 2022, **16**, 15072–15085.

54 Y. Yao, J. Yang, Q. Gu and Y. Zhai, *Rear-view Vehicle Detection Based on MSER and Spatial Combination Feature Description*, SPIE, 2016.

55 B. Colzani, L. Pandolfi, A. Hoti, P. A. Iovene, A. Natalello, S. Avvakumova, M. Colombo and D. Prosperi, *Int. J. Nanomed.*, 2018, 957–973.

56 F. Cao, Y. Xu, Y. Guan, K. Zhang, H. Qiu, Z. Xu, Y. He, Z. X. Xiao, G.-F. Zha and J. Pang, *J. Nanobiotechnol.*, 2025, **23**, 523.